Case Studies in Thermal Engineering 28 (2021) 101523

Contents lists available at ScienceDirect

Case Studies in Thermal Engineering

journal homepage: www.elsevier.com/locate/csite

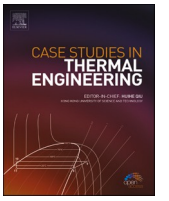

Experimental study on breakup mechanism of microbubble in 2D channel

Chang Hun Lee [a], Somchai Wongwises [b,c,**], Dong-Wook Jerng [d], Ho Seon Ahn [a,e,f,*]

[a] Department of Mechanical Engineering, Incheon National University, Incheon, Republic of Korea
[b] Department of Mechanical Engineering, King Mongkut's University of Technology Thonburi, Bangkok, Thailand
[c] National Science and Technology Development Agency (NSTDA), Pathum Thani, 12120, Thailand
[d] School of Energy Systems Engineering, Chung Ang University, Seoul, Republic of Korea
[e] Nuclear Safety Research Institute, Incheon National University, Incheon, Republic of Korea
[f] AHN Materials INC, Incheon, Republic of Korea

ARTICLE INFO

Keywords:
Microbubble
Venturi nozzle
Bubble visualization
Break-up mechanism
2D channel

ABSTRACT

The breakup mechanism of a microbubble in a 2D channel, was studied through visualization experiments. A venturi-shaped nozzle made with a 3D printer in a 2D channel was employed, and the pressure data and visualization images were analyzed. It is compared that he bubble behavior and size distribution according to the change in the rear-end exit angle of the venturi-shaped nozzle. As the exit angle increased, the bubble size decreased. However, it was confirmed that wake flow was formed in the venturi channel with an exit angle above 20°. By analyzing the visualization, we confirmed that the air bubbles interacted with the central flow and split into pieces. To maximize this process, a flare-shaped diffuser was designed and evaluated. The bubble breakup performance of the flared diffuser was better than that of the linear exit angle, in terms of the bubble size. It was a flared diffuser that satisfied the conditions for maximizing the bubble breakup process in a water flow rate of (35 L/min) and an air flow rate (0.1 L/MIN) experiments. Based on the results, it is expected that the limitations of the venturi-shaped microbubble generator can be overcome.

1. Introduction

We observe different forms of air bubbles when drinking beverages, raising fish in fish tanks, or when watching waves on the beach. However, microbubbles can be named when the bubbles are so small that they cannot normally be seen (micrometer-order or less). Small bubbles are classified as microbubbles or nanobubbles because they have characteristics that are different from those of normal bubbles. Microbubbles with the same volume as normal bubbles have a comparatively larger interface area (liquid-gas). This feature is particularly effective in industrial fields [1,2]. This is because the increase in the interface is advantageous in terms of chemical reactions and heat and mass transfer. Additionally, microbubbles have very small buoyancy owing to their small size (volume). Because of this, the microbubbles rise toward the water surface like a normal bubble, but its velocity (less than 1 mm/s) is very slow, so it stays in the water for a long time. Microbubbles of a certain size (less than 50 μm) gradually contract and eventually disappear in the water.

* Corresponding author. Department of Mechanical Engineering, Incheon National University, Incheon, Republic of Korea.
** Corresponding author. Department of Mechanical Engineering, King Mongkut's University of Technology Thonburi, Bangkok, Thailand.
E-mail addresses: somchai.won@kmutt.ac.th (S. Wongwises), hsahn@inu.ac.kr (H.S. Ahn).

https://doi.org/10.1016/j.csite.2021.101523
Received 22 July 2021; Received in revised form 18 September 2021; Accepted 30 September 2021
Available online 2 October 2021

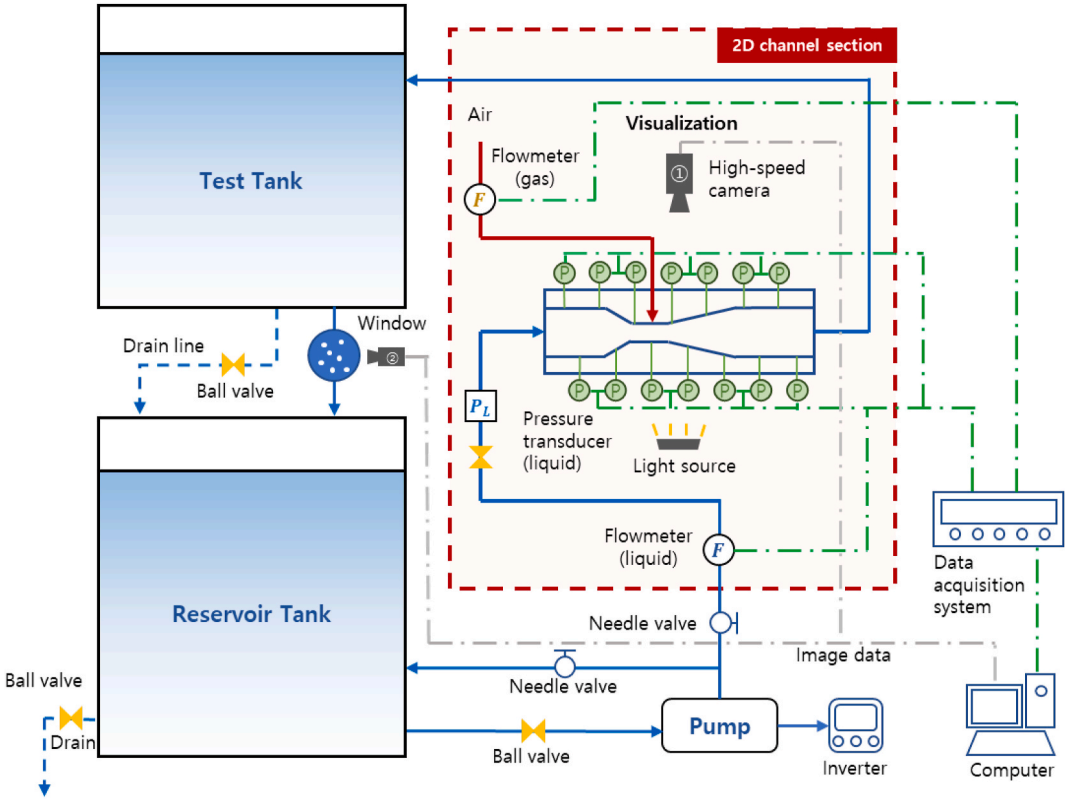

Fig. 1. Schematic of microbubble generation experimental facilities.

This is because the internal gas dissolves in the surrounding water because of the high pressure inside the bubble. As the bubble shrinks, the pressure inside the bubble increases. This process is repeated and accelerated, and the bubble finally disappears [3–5]. The relationship between the bubble diameter and the pressure follows the Young–Laplace equation:

$$P = P_1 + 4\sigma/d$$

where P is the gas pressure, P_1 is the liquid pressure, σ is the surface tension of the liquid, and d is the diameter of the bubble.

Microbubbles can be applied to the green algae phenomenon and the agricultural and fishery industries by supplying oxygen to the water. Additionally, free radicals generated when disappear in water kill bacteria and viruses. Furthermore, in the process of wastewater treatment, contaminants can be separated and removed by adsorbing, and the floating contaminants, and oxygen supply for microbial activation in the microbial aeration tank can be performed because the microbubbles have an electric double layer on the surface [6–8].

In response to a demand for such microbubbles, a method for generating microbubbles has been developed in various forms according to various principles such as, decompression, rotation, gear, and nozzle methods [9–15]. However, except for the nozzle method, the other methods require a condition to create a air-water two-phase flow before the process of splitting the air bubbles. Additionally, these methods are inefficient in terms of energy consumption because of the large pressure drop. Additionally, the structure is complicated because the gears or impellers inside the device that are used for splitting air bubbles rotate [11,17].

The nozzle method can self-absorb air by using a static pressure lower than the atmospheric pressure formed by the shape of the nozzle. Therefore, it is possible to easily form a two-phase flow without any additional air input devices. Therefore, the nozzle method is structurally simple, and is advantageous for installation convenience and maintenance. In particular, the venturi-type generator is excellent in terms of energy efficiency because the power consumed to induce the air flow is low owing to a small pressure drop, and moving parts are not required inside the device.

For microbubbles to be applied to various applications, the bubble size, distribution, and density are proposed as important parameters. This is because a suitable bubble size and a sufficient amount bubbles of that size are required to perform the role of microbubbles in an application. In this sense, conventional venturi-type microbubble generators cannot sufficiently break air bubbles, making it difficult to generate dense microbubbles. Additionally, to create a small microbubble measuring tens of micrometers, a method for increasing the flow rate uses a method called cavitation [16]. This is a method for increasing the power consumption, and is not a good method but is used as a temporary expedient to diminish the existing advantages of the nozzle-type microbubble generator [10–12,18].

In this study, a venturi-type microbubble generator suitable for use in various applications of microbubbles was investigated. To

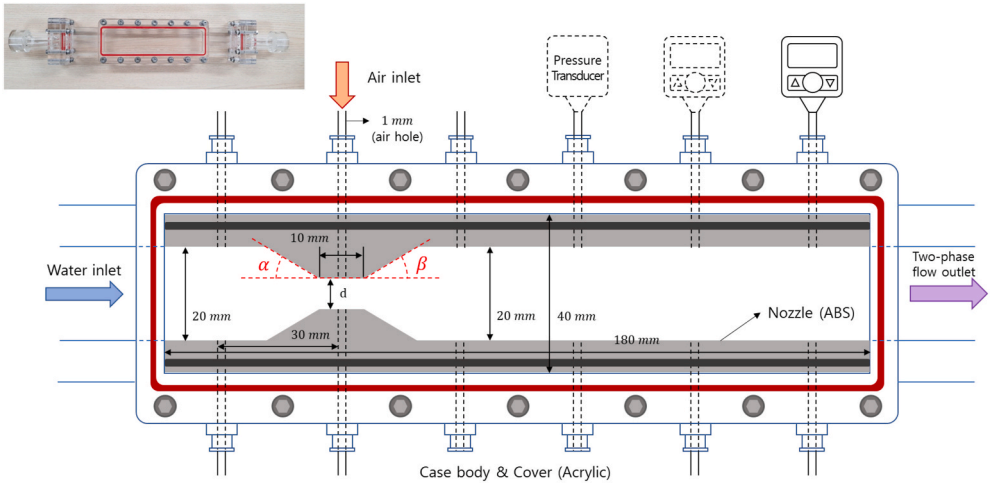

Fig. 2. Schematic of test section and picture.

overcome the limitations of the venturi-type generator, a thorough understanding of the complex bubble dynamics and bubble breakup mechanisms occurring within the nozzle is essential.

In this study, a symmetrical 2D rectangular nozzle was fabricated to observe the bubble dynamics in a general 3D cylinder-type Venturi nozzle in detail. In previous studies [19], it was found that the bubble breakup occurred in the section where the air bubble introduced from the nozzle neck expanded the flow path. This bubble breakup phenomenon, which is necessary to understand the causal relationship between the nozzle shape and the bubble size and distribution, was observed in detail. Jiang Huang et al. confirmed that the bubbles close to the side wall experienced severe deformation in the diverging section at low flow rates [20]. Through this, it was argued that shear stress plays an important role in bubble breakage. On the other hand, it was argued that the interaction between the turbulent vortex and the bubble was strengthened at high flow rates, which played a dominant role in the bubble break-up phenomenon. Liang Zhao et al. paid particular attention to the bubble behavior [21]. By observing the bubble position over time, the velocity and acceleration of the bubble were obtained. Through this, it was confirmed that the bubble experienced a sharp deceleration due to the large acceleration in the diverging section. It is argued that this is due to the pressure recovery due to the increase in the cross-sectional area of the flow path in the diverging section and plays a key role in the bubble break-up phenomenon. Since the 2D structure has an additional wall above and below the flow path, it is not 100% consistent with the phenomenon in the 3D nozzle. Nevertheless, the breakup mechanism was confirmed by photographing the bubble behavior in the section in which the flow path was expanded, by using a high-speed camera. Furthermore, we proposed a nozzle structure that can maximize the breakup effect in a Venturi nozzle by using the captured image. It is expected that the commercialization of microbubbles will be accelerated by this study.

2. Experimental

2.1. Experimental facilities

2.1.1. Microbubble experimental loop

The experimental device is a closed loop, as illustrated in Fig. 1, and the working fluid (tap water) from the reservoir tank (2000 L) moves to the test tank (1120 L) through the test section (2D channel section) with other fluid measuring equipment. Then, the microbubbles in the fluid are removed, and the fluid returns to the reservoir tank. The experimental apparatus is divided into a fluid transfer part, a data collection part, and a nozzle part, the details of which are as follows:

The fluid transfer part serves to transfer fluid in the loop, such as two water tanks (test tank and reservoir tank) and pumps (7.5HP*2 motor, 400 L/min maximum flow rate, 120 m maximum head), valves, and pipelines. The blue line represents the flow path of the liquid (water), and the red line represents the flow path of the gas (air). Water is transported from the reservoir tank to the test section by a pump, and the air is injected or self-absorbed into the nozzle owing to the pressure difference between the outside and the test section. A turbine flowmeter was installed between the pump and the test section to measure the flow rate of the fluid, and a volumetric flowmeter was installed in the air line. Several pressure transducers were mounted longitudinally at equal intervals in the nozzle to compare the pressures at different locations in the test section. The data of these measuring instruments were collected using a data acquisition system and recorded on a computer. This is represented by a green line in Fig. 1. Visualization was conducted in two places, as illustrated in Fig. 1. First, the 2D channel section represented by red dotted line was photographed by using a high-speed camera. The bubble behavior was visualized in detail by placing a light source on the side facing the camera. The second is to analyze the size and distribution of bubbles by taking the microbubbles introduced in the test tank into a separate visualization section and then photographing them. The visualization data were transmitted to a computer for analysis and is represented by the gray lines.

Table 1
Preliminary experiment cases under cavitation conditions.

Nozzle neck width, D_{neck}, mm	3	4	5	6	7	8	9
Inlet channel width, $D_{channel}$, mm	20 (depth = 5 mm)						
Area Ratio (A_{neck}/ $A_{channel}$)	0.15	0.2	0.25	0.3	0.35	0.4	0.45

As described above, both the flow and the visualization data were transmitted to a computer and analyzed organically together, which is represented by the chain line in Fig. 1.

2.1.2. Test section

The test section where the microbubbles occurred was made of transparent acrylic in the form of a square channel. As illustrated in Fig. 2, there are inlets/outlets on the left and right sides of the main body through which water can enter and exit. The water introduced into the inlet flowed through the nozzle. At this time, it comes in contact with the air introduced from the neck of the nozzle, becomes a bubbly flow and flows out to the outlet. The total length of the channels inside the nozzle is 180 mm, and the width is 40 mm. There are six points where the air hole is connected to the pressure transducer and are arranged at 30 mm intervals. In the experiment, the nozzle was mounted inside the body, and a cover and an O-ring covered the body and sealed the device. Therefore, the device is set up to test one case.

The nozzles forming the flow path in the channel are made of acrylonitrile-butadlene-styrene material in the top and bottom using a 3D printer. The nozzle is 5 mm thick, and the width at the front and rear ends of the nozzle, excluding the nozzle neck, is 10 mm. Since the width of the channel is 40 mm, the width of the flow path at both ends is 20 mm, and the cross-sectional area of the inlet and outlet of the body is the same as 20 mm × 5 mm ($A_{channel}$). The nozzle is a venturi-type, divided into a contraction section, a nozzle neck, and an expansion section, where the flow path is narrow at the front end, narrowest at the nozzle neck and widens again at the rear end. The length of the nozzle neck is 10 mm, and the air hole is located in the center and is 1 mm in diameter. The experimental cases are determined according to the size of the nozzle neck, the angle of the reduction section, and the enlargement section. Since the nozzle is manufactured by a 3D printer, it can be printed (manufactured) in various forms, allowing various path shapes to be tested. The main velocity component of the fluid flow is the axial velocity (U_X). Except for the wake region, the axial velocity (U_Y) of the main flow ranges from 0.5 m/s to 14.6 m/s depending on the flow conditions. As the fluid enters the diverging section, the Y-axis velocity (U_Y) develops along the flow path to a width of 20 mm. On the other hand, since the Z-axis direction depth is kept constant at 5 mm, the Z-axis direction $U_Z$has a relatively small size. Considering that the size of the bubble introduced from the air hole is 2∼3 mm at low flow rate, the depth was selected as 5 mm. This is because, if the depth of the flow path is smaller than the size of the bubble, it will move away from the shape of the sphere and the exact size cannot be measured only with the cross-sectional image. In summary, in this experiment, depending on the flow parameter and the geometric parameter, it is not clear how narrow the flow path must be to be considered a 2D channel. However, since the velocity component U_Z is relatively small, it was considered as a 2D channel for observing bubble behavior and bubble break-up in the diverging section.

2.2. Experimental methods

A Venturi nozzle refers to a form in which the cross-sectional area of a pipe is narrowed and then widened; when the flow inside the pipe passes through a narrow cross-sectional area, it generates a Venturi effect in which pressure decreases. This can be explained using the Bernoulli's theorem. In the case of steady, incompressible, and inviscid flows, according to the principle of mass continuity, when the fluid passes through a narrow cross-sectional area, the velocity of the fluid increases, and with the conservation of mechanical energy, the static pressure also decreases. The following is Bernoulli's equation:

$$\frac{v^2}{2} + gh + \frac{p}{\rho} = \text{constant}$$

where v, g, h, p and $\rho$are the liquid velocity, gravity, elevation head, static pressure of the liquid, and liquid density, respectively. Since there is no change in the height, the change in the velocity eventually induces a change in the pressure. When using a static pressure that is less than the atmospheric pressure because of an increase in the flow velocity, air is introduced into the nozzle by itself, owing to the pressure difference. Depending on the geometrical parameters, such as the ratio of the cross-sectional area of the nozzle neck to the inlet, and the flow parameters such as the water flow rate, the decreasing static pressure at the nozzle neck and the amount of incoming air vary [22].

However, if the fluid flow rate is too high or the nozzle neck is too narrow, the static pressure at the nozzle neck becomes very low. If this pressure becomes smaller than the vapor pressure of water, cavitation can occur. This is because the fluid flow rate and the size of the nozzle neck are parameters that can affect the bubble size, and their values are extreme conditions in which cavitation occurs. However, because some of the generated bubbles are vapor bubbles that will quickly disappear, it is difficult to expect effects such as an increase in dissolved oxygen amount and sterilization. Although cavitation can help bubble breakup, its effect is not significant. Rather, it is a loss in terms of energy efficiency owing to the additional pressure drop. Cavitation is a phenomenon that should be avoided because it causes serious damage to the impeller, including the inner surface of the nozzle.

Table 2
Exit angle cases for diffuser.

Exit angle, β, [°]	5	7	10	15	20	30	45
Area Ratio (D_{neck}/ $D_{channel}$)	0.2 (D_{neck} = 4 mm)						
Angularity (tan(β)* 100), [%]	8.75	12.28	17.63	26.79	36.40	57.74	100

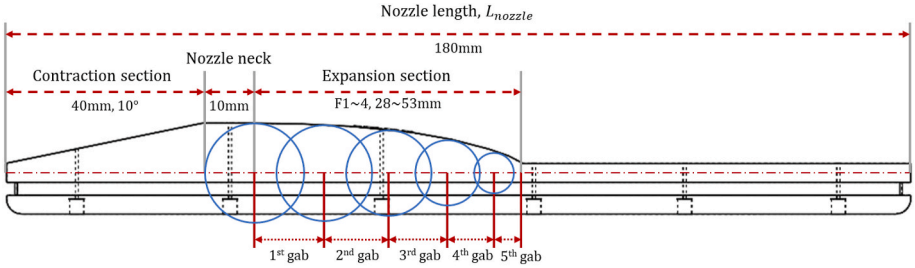

Fig. 3. Schematic of flared diffuser nozzle.

Table 3
Design specifications of flared diffuser nozzle.

Unit(mm)	Circle diameter	F1	F2	F3	F4
1st gab	18.4	8.8	10.8	12.5	13.9
2nd gab	17.8	6.8	9.6	11.3	12.9
3rd gab	15.8	5.2	8	10.1	11.8
4th gab	12	4	4.6	6.5	9.3
5th gab	7.4	3.7	3.8	4.7	5
Expansion section length		28.5	36.8	45.1	52.9

2.2.1. *Preliminary experiments*

Since the 2D channel experiment has a constant channel depth unlike 3D nozzle, a smaller diameter ratio is required to make the area ratio of the self-absorption condition. In this study, the air flow rate was regulated to 0.1 L/min to secure the data of two-phase experiments over a wide flow range. To compare and analyze various flow path shapes in the diffuser section where the flow expands, such as the exit angle at the rear end of the nozzle, an appropriate nozzle neck width is selected. Table 1 presents an experimental case to determine the width of the nozzle neck. The nozzle neck width was tested from 3 mm to 9 mm, which means that if the inlet channel width is 20 mm, the area ratio is tested from 0.15 to 0.45. The water flow rate was adjusted from 5 L/min to 35 L/min in 3 L/min intervals, and the pressure data were collected. The flow inside the nozzle was inferred by analyzing the collected pressure data.

2.2.2. *Experimental cases*

Both the flow parameters and the various geometric variables in the nozzle affect the microbubbles. The flow path expansion section where the bubble breakup occurs, i.e., the shape of the diffuser, is of particular interest in this study. For this, the other parameters are fixed as follows: In all cases, the inlet channel width was 20 mm. The depth was 5 mm, the length of the nozzle neck was 10 mm, the diameter of the air hole located in the center was 1 mm, and the contraction angle was 10°.

As can be seen in Table 2, microbubble generation experiments were performed at nozzle exit angles of 5°, 7°, 10°, 15°, 20°, 30°, and 45°. The water flow rate varied from 5 L/min to 35 L/min, and the air flow rate was fixed at 0.1 L/min. The static pressure was measured using pressure transducers at six points toward the fluid flow. The flow inside the channel was visualized at a speed of up to 8000 fps using a high-speed camera. Additionally, a separate section for measuring the size and distribution of the bubbles was provided in the test tank.

By analyzing the pressure data and the visualized image obtained through the exit angle experiment, the advantages and disadvantages of the exit angle were confirmed. Using this result, we designed a diffuser shape that can maximize the advantages and compensate for the disadvantages. In this study, a flared-diffuser shape was designed as illustrated in Fig. 3. The exit angle of the nozzle neck is designed to increase slowly so that the bubble breakup for microbubble generation can occur more actively. The shape of the diffuser is based on circular arcs of five sizes, and the cases are selected according to the gaps between them. The centers of the circles are located on the center line 1.85 mm away from the nozzle wall. In the F1 case, the gap between the circles is the smallest, and thus it has a sharp gradient. It is a total of four cases, and the gaps increase gradually until the F4 case. As presented in Table 3, the first of the circles is the largest and becomes smaller, and the spacing tends to be the same.

2.2.3. *Visualization methods*

As illustrated in Fig. 1, visualization in the experimental facility occurs in two sections. In one section, microbubbles are taken

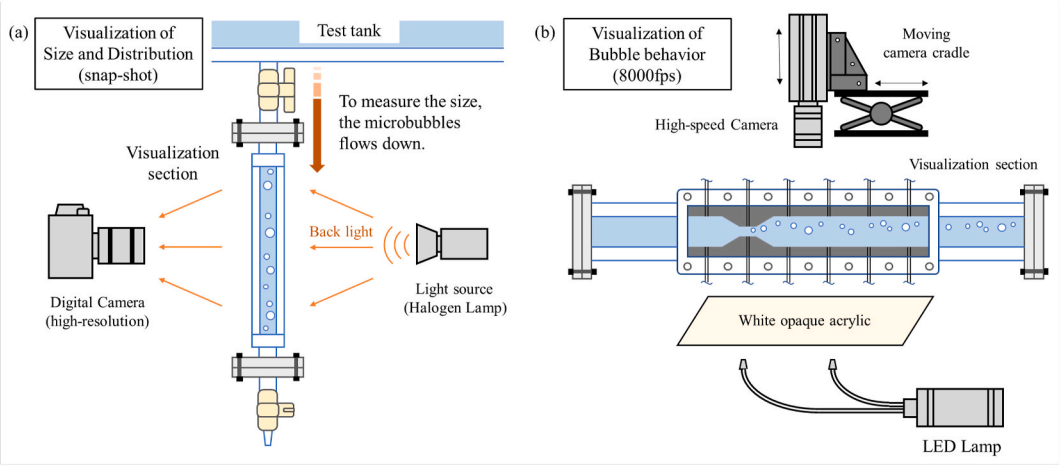

Fig. 4. Visualization methods for microbubble (a) size distribution and (b) bubble behavior.

snapshots of in the visualization section installed at the bottom of the test tank. In the second section the microbubble behavior is observed in the test section using a high-speed camera. The detailed specifications of these two visualization methods are as follows.

1. Snapshot visualization with high resolution (Nikon D5500: Effective pixels of 24 million pixels, image size of 4,928x3,264 pixels): The size distribution of microbubbles
2. High-speed visualization (8000 fps, 1024x372 of pixels): The bubble breakup mechanism from bubbly flow to microbubbles

As illustrated in Fig. 4 (a), regarding microbubble size observation, the visualization section installed at the bottom of the test tank is a transparent acrylic box, and the inner space where the microbubbles are filled is 100 mm*100 mm in width*length and 10 mm in depth. The composition is a backlight facing the light source (halogen lamp), and the camera shoots the shadow of the bubble, and the snapshot is taken with a high-resolution digital camera.

High-speed visualization of the test section was performed to observe the bubble breakup mechanism. As illustrated in Fig. 4 (b), an LED lamp was used as a light source, and a backlight composition was used to accurately observe the bubble behavior and breakup process. A white, opaque acrylic filter was placed between the light source and the test section body to spread light evenly to the channel of the test section. Because the channel is narrow and long, it is necessary to set the camera from a long distance when capturing the entire scene, and closer when the bubble breakup is observed closely. Therefore, a camera cradle was made so that the camera could be moved up and down as well as back and forth (longitudinal direction).

After capturing high-resolution images of the microbubbles, the background image was erased by enhancing the contrast. The image was then converted to monotone, by using a commercial image processing tool (ImageJ) and was used on the microbubble interface to erase the residual pixels around the air bubbles to perform the post-processing, as illustrated in Fig. 5. The resolution (L_{res}) of this snapshot is 3.83 μm per pixel through the scale of the reference ruler. The maximum error of bubble size measurement through the resolution of this snapshot is as follows.

$$E_{max} = \left(L_{rew}/D_{b,\,min}\right)^{*}(100(\%)) = 19.15\%$$

Finally, the microbubble size distribution was quantified and compared case by case, as illustrated in Fig. 6.

3. Results and discussion

3.1. Pressure distribution

3.1.1. Nozzle width variation

As described above, in the microbubble generation experiment, the pressure was measured at a total of six points. The distance between each point was 30 mm, and the position of the second point was at the center of the nozzle neck, where the air hole was located, there was another point 30 mm from the second point toward the nozzle inlet. The outlet direction is present one-by-one each time the four points fall by 30 mm.

Fig. 7 presents the pressure distribution at each point according to the variation in the width of the nozzle neck. The water flow rate was 35 L/min, which was the highest in the experimental range. Because the fluid that arrives through the outlet of the nozzle is the free water surface of the water tank, assuming that the outlet pressure is the same, the pump increases the pressure of the pump by the amount of pressure drop generated by each nozzle. This is because the pump delivers the same flow of the working fluid within its capabilities. As a result, the pressure loss at the nozzle can be inferred from the difference between the inlet pressure and the outlet pressure, and it was confirmed that the smaller the nozzle neck width, the greater the pressure drop.

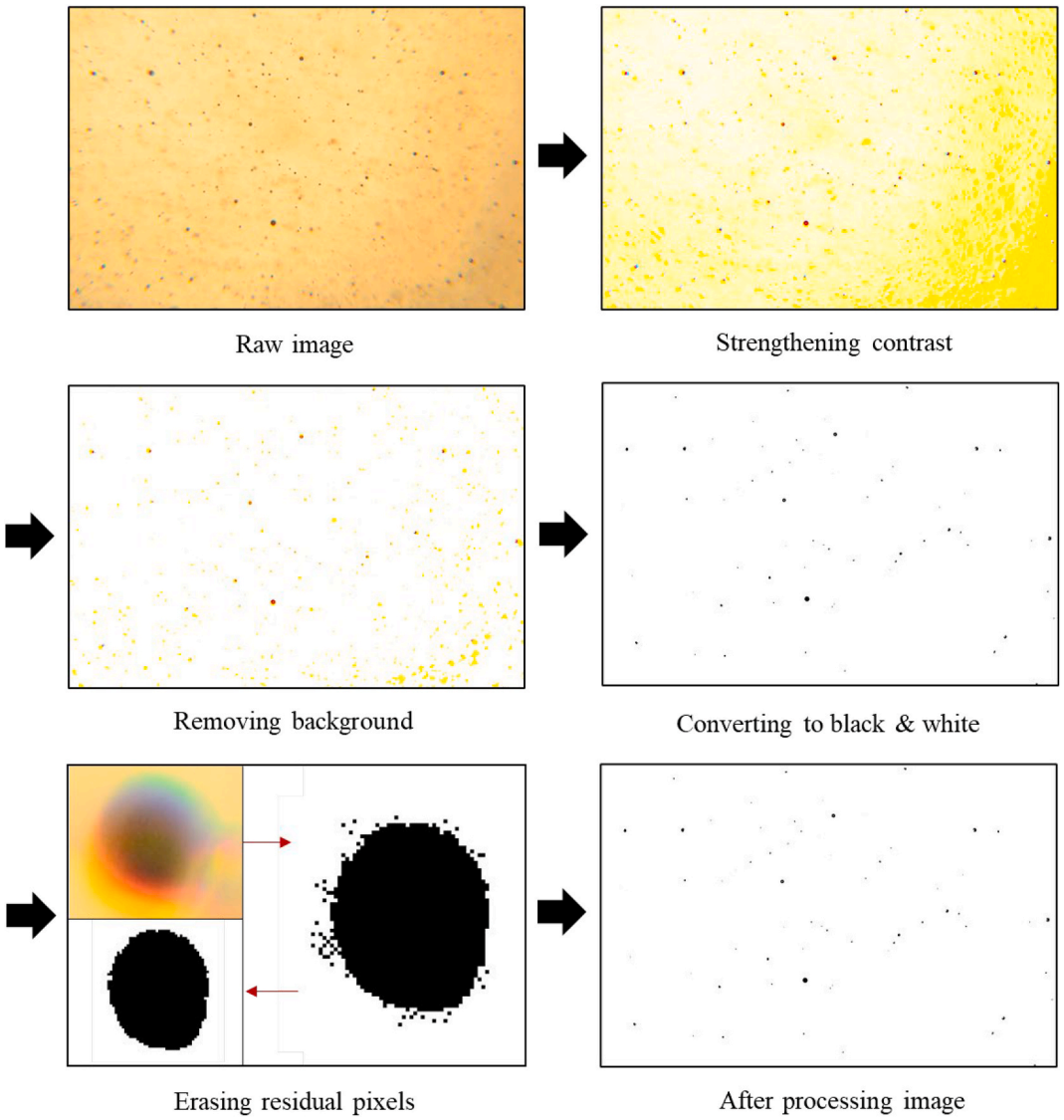

Fig. 5. Post image processing to measure the size distribution of microbubbles.

In theory, the fluid has the fastest flow rate and the lowest pressure at the neck of the nozzle with the narrowest flow path. However, if the flow is not fully developed, the fluid flow will not follow the diffuser shape in the section where the flow path is expanded, and the main flow goes straight because of inertia. Additionally, the pressure gauge used in this experiment was installed in a tube connected to the wall to avoid disturbing the flow. Therefore, the pressure was measured at the lowest point of 30 mm. Then, the pressure reduced by the high flow velocity at the nozzle neck recovered as the flow velocity reduced, excluding the loss of pressure as the flow path expanded. Therefore, compared with the pressure at points 4, 5, and 6, where the pressure was restored, the relatively low pressure at point 3 was confirmed. At point 3, the pressure difference between the 5- and 8-mm nozzle width cases was approximately 10 kPa, which is within the error range. On the other hand, the pressure difference between the 3- and 4-mm nozzle width decreased noticeably from 30 to 40 kPa. The area ratio compared to the cross-sectional area at the inlet is 0.2 or less, which requires a larger area ratio than that required in previous 3D nozzle studies. However, in the 3 mm nozzle width case, when the area ratio (0.15) was too small, the pressure at point 3 increased. This is because the pressure drop owing to the loss is so great that the pressure at the inlet end (point 1) is extremely high. As a result, the pressure at the nozzle neck rises together, which damages the pressure difference induced by the nozzle shape. This has a negative effect on the self-absorption of air. As a result, a 4-mm nozzle neck case was selected as the basic case, which induces the lowest pressure at the nozzle neck, which is highly likely to self-absorption, and the pressure at the inlet end is not too large. Here, the contraction angle is 10° and the exit angle is 5°.

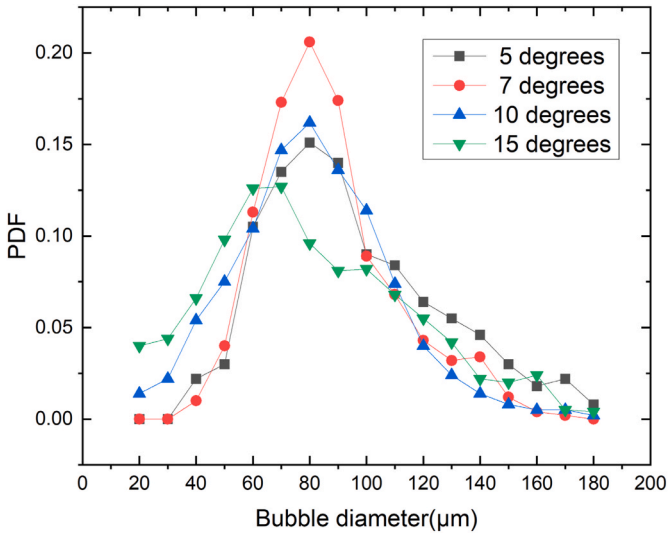

Fig. 6. Microbubble size distribution.

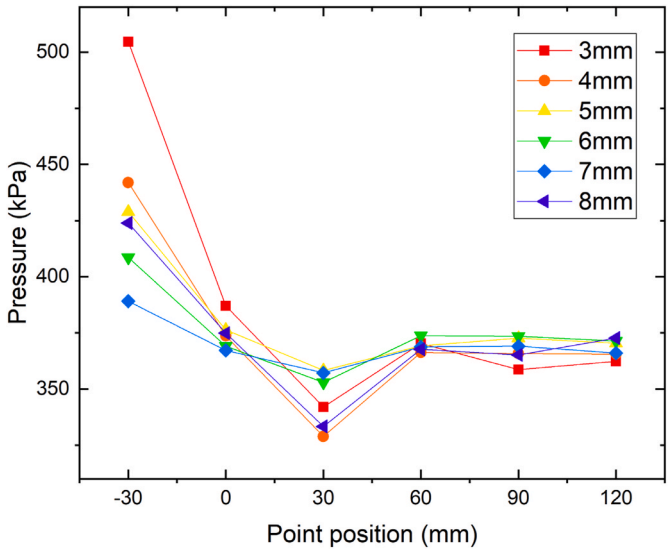

Fig. 7. Pressure distribution with nozzle neck width variation.

3.1.2. Exit angle variation

As confirmed in a previous study [19], as the fluid (water) flow rate increases, the pressure drop increases. As illustrated in Fig. 8, the pressure graph for each exit angle exhibits the same trend. Additionally, the pressure drop increases as the exit angle increases. When the water flow rate was low, no significant difference was observed. However, it gradually increased as the water flow rate increased, showing a distinct difference from 20 L/min or higher.

In a nozzle, such as a Venturi nozzle, where the width of the flow path becomes narrower and then widens, the fluid may not accurately follow the flow path. This is more pronounced as the fluid velocity increases, and the flow path widens rapidly. Therefore, the high-speed main flow passing through the narrow flow path does not follow the rapidly widening flow path and proceeds straight because of inertia. The wake flow separated from the main flow occupies the place between the main flow and the wall of the wider flow path and forms a wake region. The resulting loss appears as a pressure drop, and this process generally intensifies the exit angle.

In Fig. 9 shows the pressure change according to the exit angle at each point. The pressure changes according to the exit angle vary for each point in the nozzle. The water flow rate is 35 L/min, and the air flow rate is equal to 0.1 L/min. The amount of pressure drop was confirmed by the flow rate in the previous graph, and this graph presents the data at a high flow rate (35 L/min) and presents the pressure changes according to each point. In detail, the pressure changes by point according to the change in the rear end angle can be divided into three groups according to the trend. The first group was 5°, 7°, and 10° (Fig. 8 (b)). In this group, the pressure difference at

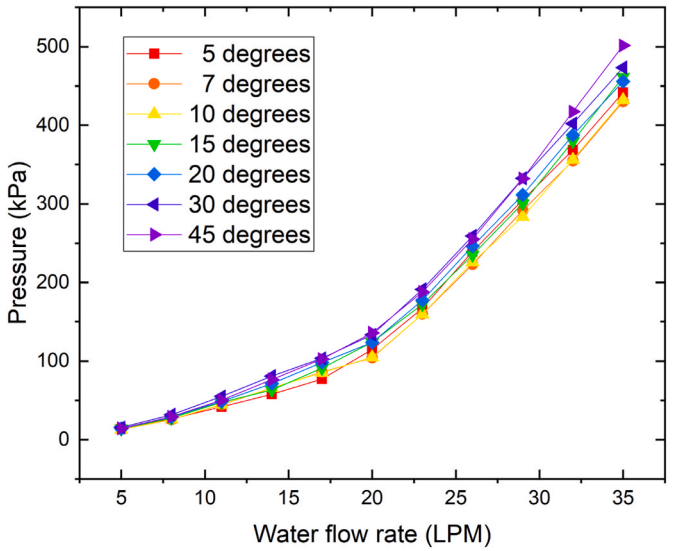

Fig. 8. Pressure variation according to water flow rate by exit angle.

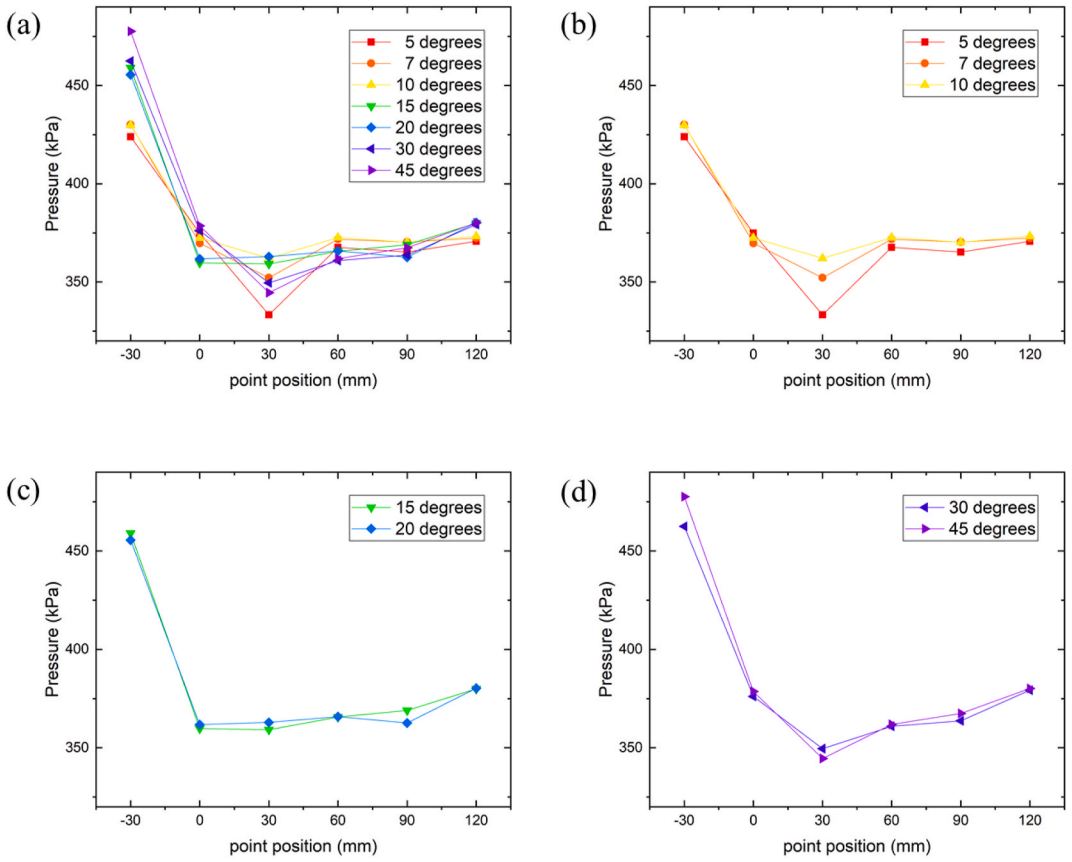

Fig. 9. Pressure distribution by exit angle variation.

point 1 was approximately 7 kPa, which was similar within the error range. This result indicates that the wake flow that affects the pressure drop did not occur significantly up to 10°. Additionally, at point 3, the pressure tended to increase as the angle increased. This trend is also observed in the second group, at 15° and 20°. Because the fluid follows through the flow path well, as the exit angle increases, the cross-sectional area of the flow path increases, and as a result, the flow velocity decreases, and the pressure increases. As

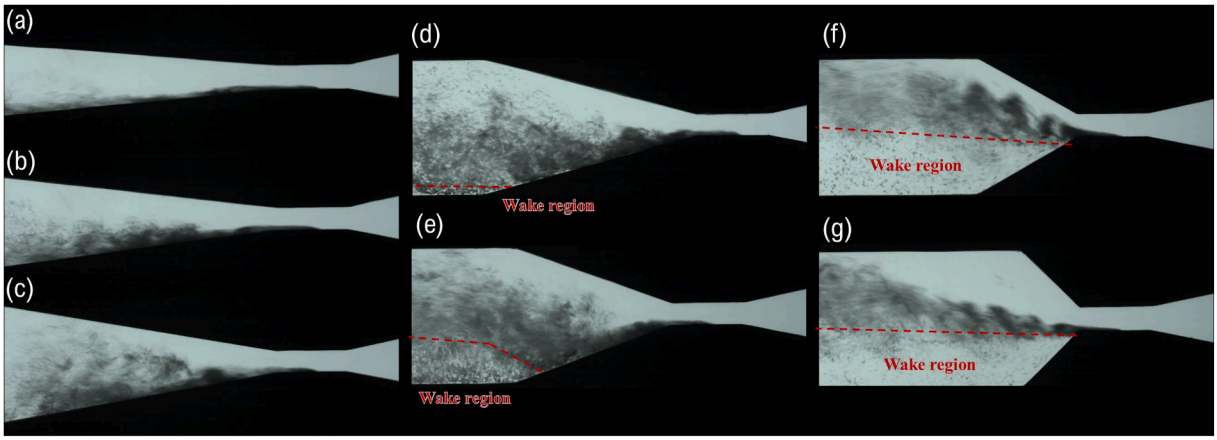

Fig. 10. Visualization image of two-phase flow by the exit angle. (a) 5°, (b) 7°, (c) 10°, (d) 15°, (e) 20°, (f) 30°, and (g) 45°.

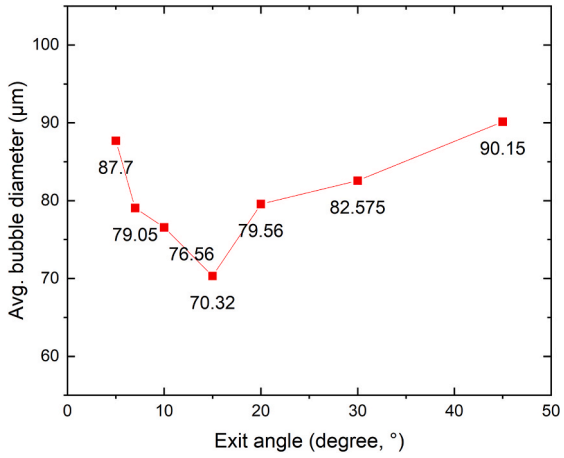

Fig. 11. Average bubble size according to exit angle change.

the reduced pressure recovers owing to the increase in the flow rate, the pressure after point 4 appears to be similar. However, in the third group, at 30° and 45°, the pressure at point 3 is the lowest among all cases except at 5°, and the pressure tends to recover slowly toward the rear end. This is because a perfect wake region is formed in the expansion section after the nozzle. In the third group, the main flow passing through the nozzle goes straight ahead without following the wall of the channel, which is widened by inertia. Accordingly, the main flow excluding the wake region flows as if passing through a flow path that is smaller than the cross-sectional area of the actual flow path. Therefore, the flow rate of the main flow was maintained at a certain level, and the pressure could not be recovered; thus, it showed a low pressure at point 3. As the fluid flowed to the rear end, the main flow developed slowly, and the pressure slowly recovered and increased. In the second group, this trend was confirmed at point 6, suggesting that a certain part of the wake flow had occurred. For a more detailed insight, the following visualization images were used:

Fig. 10 illustrates the bubble behavior according to the change in the exit angle. At 5°, 7°, and 10° of the first group, bubbles occasionally bounced to the center of the flow with a high velocity, but it was confirmed that the bubbles followed the wall of the flow path well (Fig. 9 (a), (b), and (c)). In the second group, at 10° and 15°, it seems to follow the set flow path well in the expansion section, but the eddy starts to occur at the end of the expansion section (Fig. 9 (d), (e)). In the third group, at 30° and 45°, the air bubbles do not follow the wall of the expansion section. The main flow, which moves with the bubbles, travels straight because of inertia and develops slowly (Fig. 9 (f), (g)). Fig. 10 presents the bubble behavior according to the change in the exit angle. The flow conditions are 35 L/min of fluid flow and 0.1 L/min of air flow. At 5°, 7°, and 10° in the first group, the bubble generally follows the wall well with water (Fig. 9 (a), (b), and (c)). However, the air bubbles start to break gradually owing to the shear stress caused by the difference in velocity between the center of the flow path and the wall. This trend was also observed in the second group (Fig. 9 (d), (e)). On the other hand, in the third group, only a small amount of breakup occurred between the main flow and the wake region because the air bubbles followed the main flow (Fig. 9 (f), (g)). In the case of the second group, at 10° and 15°, the bubble seems to follow the wall of the expanding flow path, but the eddy begins to occur at the end of the expansion section. In the third group, at 30° and 45°, the air bubbles cannot follow the wall of the expansion section and develop little by little while going straight because of inertia. The wake region

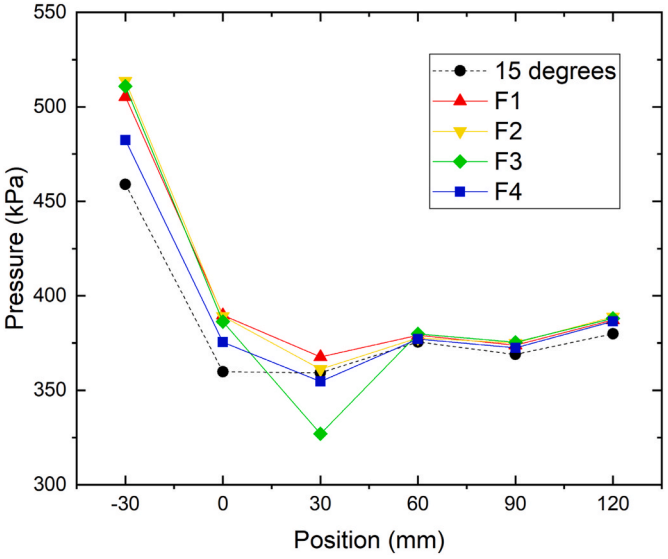

Fig. 12. Pressure distribution of flared diffusers.

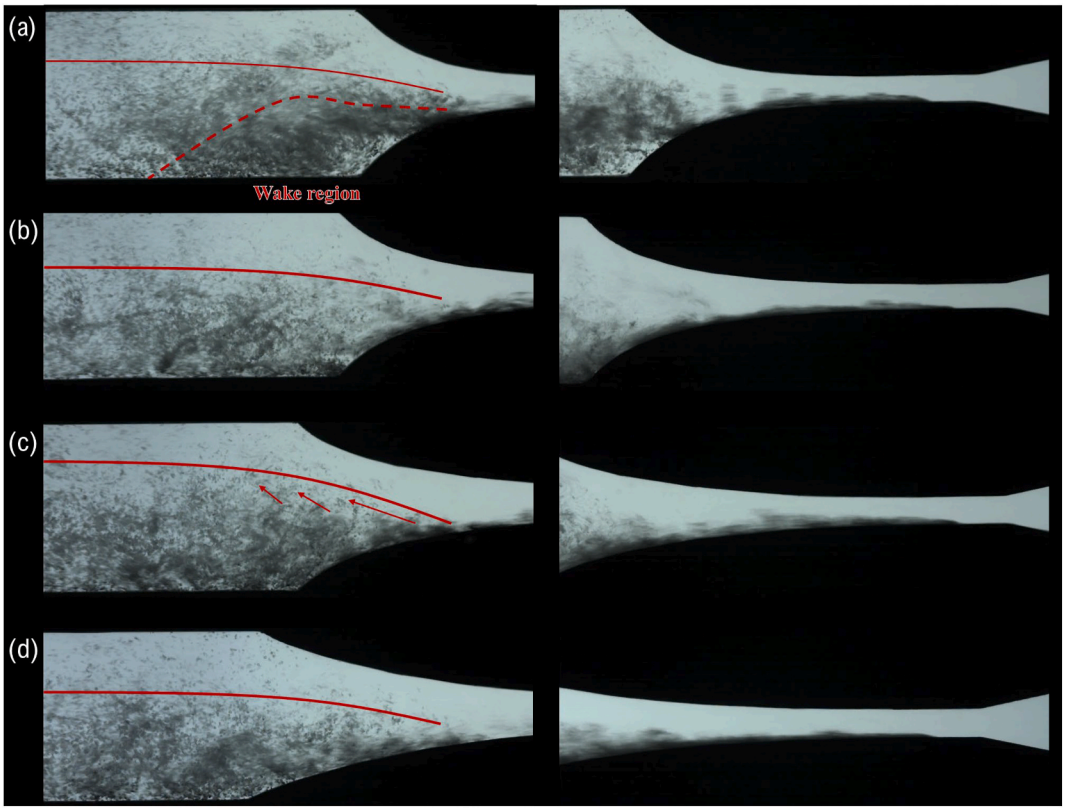

Fig. 13. Visualization image of two-phase flow of flared diffuser. (a) F1, (b) F2, (c) F3, and (d) F4.

solidifies, and the eddy in the wake region is very large and moves slowly. The air bubbles are partially broken at the boundary between the main flow and wake flow, but most of the air bubbles are carried by the main flow and quickly exit to the outlet.

Fig. 11 illustrates the average bubble size according to the angle change. In the first group, and 5°, 7°, 10°, as the angle increases, the average size of the bubbles decreases. In the third group, at 30° and 45°, a relatively large average bubble size was measured. The reason for this result is that the fluid flow did not follow the wall of the flow path. So the air bubbles exit the nozzle without breaking

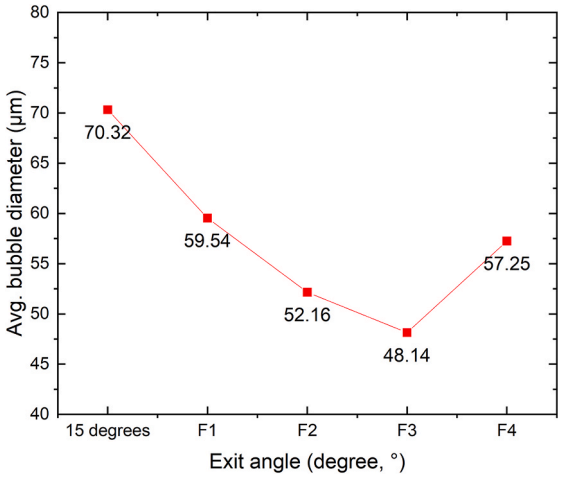

Fig. 14. Average bubble size by flared diffuser.

enough. There were many small-sized bubbles and many large-sized bubbles, the 45° case had the largest average bubble size. The second group was interesting. Out of 15° and 20°, the eddy occurs on the wall at 20°, and the average size of the air bubbles follows the trend of the third group. However, 15° recorded the lowest average bubble size of 10°. This can be explained by the location where the bubble breakup of 15° occurred. In the 20° case, as in the third group, the wake flow generated between the bubble and the wall surface does not have a significant effect on bubble breakup. However, in the case of 15°, the bubbles move along the wall to some extent, and the bubbles are broken by shear owing to the difference in the relative speed with the main flow in the center of the flow path. This breakup mechanism can also be confirmed in the 10° case, where the lowest average bubble size was recorded. As the angle increases in the first group of bubbles along the wall, this process intensifies, suggesting that bubble breakup is well performed. From the above experimental results, it was possible to infer the bubble breakup mechanism by observing the bubble behavior according to the exit angle in the expansion section of the Venturi nozzle. Additionally, the conditions for maximizing the breakup were identified (let the bubbles follow the wall and avoid wake flow, while focusing on interaction with the main flow). However, these conditions are limited in their application to angle change by a straight line. Obviously, an increase in the exit angle is one factor that intensifies the breakup phenomenon. This is because a large exit angle leads to a large pressure difference and speed difference. However, a large exit angle makes it difficult to guide the main flow and is likely to generate a wake flow. Therefore, a suitable diffuser was designed and tested to solve this problem.

Fig. 12 presents a graph comparing the pressure distribution of flared diffusers with 15° exit angle recording the smallest bubble size among the exit angle cases. In Table 3, the expansion section length was the shortest in the F1 case and increased as the number increased. At the first point (−30 mm), the pressure of the flared diffusers was measured to be greater than that with an exit angle of 15°. The pressure at the third point (30 mm) decreased gradually from F1 to F3, and then increased again at F4. As presented in Fig. 13, in the F1 case, the length of the expansion section was too short, and the change in the exit angle was rapid, resulting in a wake flow. Owing to the flare shape effect, the wake region does not lead to the outlet. Therefore, the size of the bubble exiting the wake region was broken once more. In F2, F3, and F4, where the wake flow did not occur, air bubbles generally followed the wall well. However, it is difficult for the bubble breakup to occur when the air bubbles are only on the wall. Because cavitation is avoided, it is difficult to split the air bubbles sufficiently finely with turbulence near the wall. The air bubbles moved along the wall. However, because the hydrodynamic energy of the central flow is large, the bubble breaks down as it meets this flow. Bubbles with a large size are split small by shear owing to the difference in velocity at the boundary, with the central flow and spread out widely. Because of this breakup mechanism, the F4 case has a relatively gentle angular gradient, so the interaction with the central flow is relatively small. In conclusion, to avoid wake flow, the smaller the angle change, as in F4, the more advantageous it is. To reinforce the interaction with the central flow, the gradient of the exit angle must be large, as illustrated in F1. Therefore, as illustrated in Fig. 14, F2 and F3 have a smaller average bubble size than F1 and F4, including the exit angle case.

The two-phase flow undergoes rapid changes in pressure and velocity owing to the expanding flow path. As illustrated in Fig. 15, the effect of air bubbles was confirmed by visualization of the low flow rate. For the F3 case, the water flow rate was 5 or 8 L/min and the air flow rate was 0.1 L/MIN. It is in a chronological order from the top to the bottom, and the spacing of the omitted frames between the images is entered. Bubbles introduced through the air hole maintain their shape without significant deformation when the exit angle gradient is small. However, as the exit angle gradient increased, deformation and splitting appeared. Similar to the bubble in the red circle in Fig. 15, the bubble after splitting continues to break up to a certain size or lesser.

4. Conclusion

In this study, the effect of the exit angle in a 2D channel on the generation of microbubbles was investigated. With the visualization experiment, the bubble breakup mechanism was observed and analyzed. Additionally, to maximize the breakup effect, a diffuser

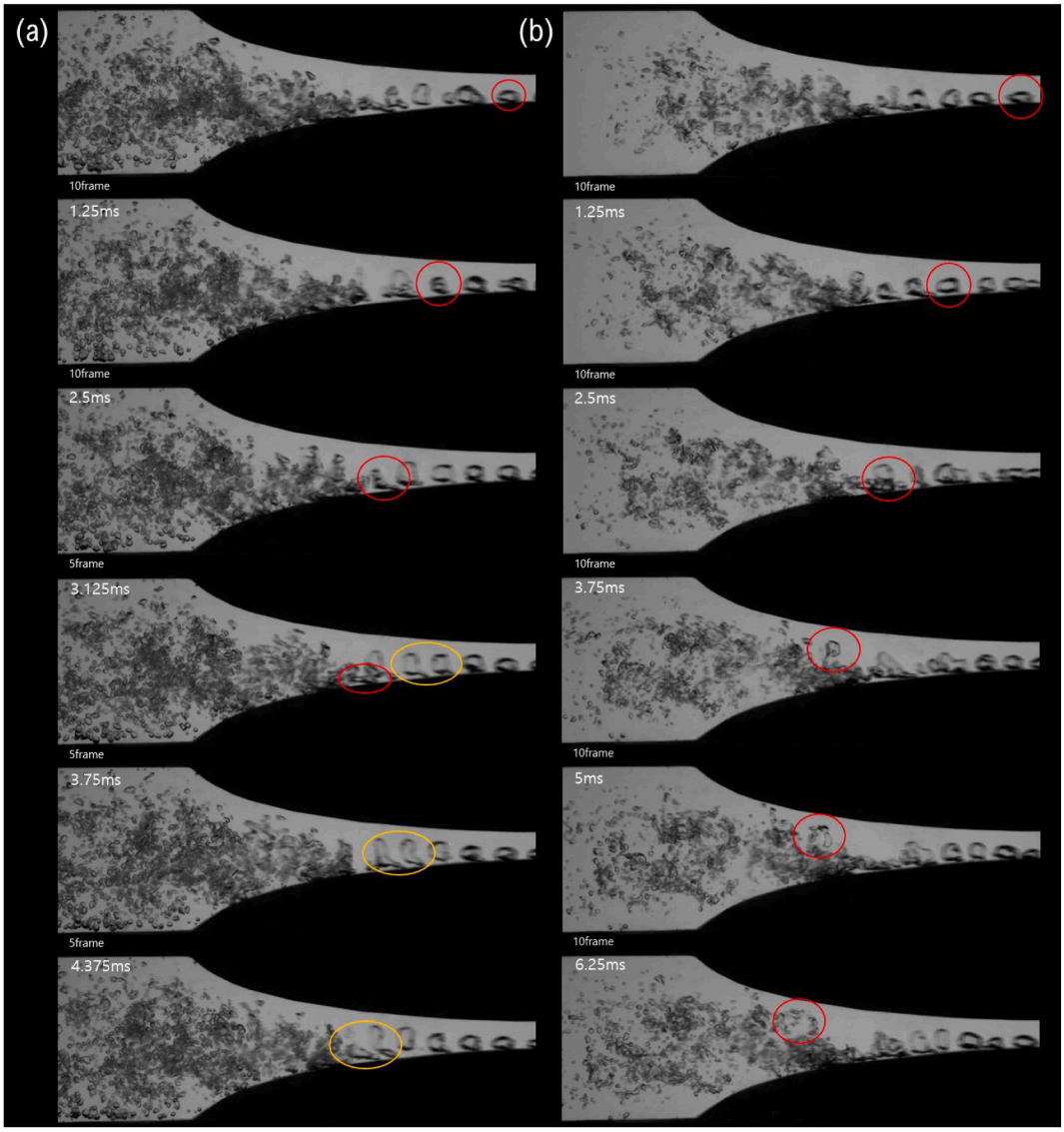

Fig. 15. Visualization image of F3 case with low water flow rate (a) 8 L/MIN, (b) 5 L/MIN.

design was proposed, and its characteristics and performance were tested.

1. As the exit angle increases, the bubbles become smaller owing to the shear stress caused by the pressure and velocity changes. However, when a wake region is formed, the air bubbles cannot follow the wall of the flow path and are not sufficiently broken. Therefore, the 15° case with relatively little wake flow occupied the lowest size with an average bubble diameter of 70.32 μm.
2. A flared diffuser was designed to cause rapid flow changes while preventing the wake flow. By moving the bubble near the center of the flow path and interacting with the central flow with a large hydrodynamic energy, the process of splitting the bubbles was confirmed. Wake flow did not occur, and the average bubble diameter (48.14 μm) of the F3 case in which this breakup process was maximized was the smallest.
3. The bubble breakup mechanism was carefully observed through low-flow visualization. The bubbles were not significantly deformed in the initial gentle expansion of the angle gradient section. Subsequently, deformation and breakup occurred in a large gradient section. The breakup continued until the bubble broke down to a certain size or less.
4. A large exit angle or a large gradient of a flared diffuser causes a strong breakup phenomenon, but suitable condition and design are required for the applicationto prevent the wake area.

Venturi-type microbubble generators have a simple structure, so they can be easily applied to various industries, however, they do not show a good performance. To overcome this problem, the breakup mechanism analyzed in this study can be used. Additionally, in

the future, various developments and applications of flared diffusers that can maximize the breakup phenomenon are expected.

Credit Author statement

Chang Hun Lee: Experiments and writing. Somchai Wongwises: Discussion, investigation and supervision. Dong-Wook Jerng: Discussion and investigation. Ho Seon Ahn: Supervision and review.

Declaration of competing interest

The authors declare that they have no known competing financial interests or personal relationships that could have appeared to influence the work reported in this paper.

Acknowledgement

The second author acknowledges the support provided by National Science and Technology Development Agency (NSTDA) under the "Research Chair Grant", and the Thailand Science Research and Innovation (TSRI) under Fundamental Fund 2022.

References

[1] S.E. Burns, S. Yiacoumi, C. Tsouris, Microbubble generation for environmental and industrial separations, Sparation and Purification Technology 11 (1997) 221–232.
[2] Akira Yoshida, Osamu Takahashi, Yorishige Ishii, Yoshihiro Sekimnoto, Yukio Kurata, Water purification using the adsorption characteristics of microbubbles, Jpn. J. Appl. Phys. 47 (8) (2008) 6574–6577.
[3] Masayoshi Takahashi, ζ potential of microbubbles in aqueous Solutions: electrical properties of the Gas−Water interface, J. Phys. Chem. B 109 (46) (2005) 21858–21864.
[4] Masayoshi Takahashi, Free-radical generation from collapsing microbubbles in the absence of a dynamic stimulus, J. Phys. Chem. B 111 (6) (2007) 1343–1347.
[5] Ashutosh Agarwal, Principle and applications of microbubble and nanobubble technology for water treatment, Chemosphere 84 (9) (2011) 1175–1180.
[6] R.T. Rodrigues, Rubio, New basis for measuring the size distribution of bubbles, Miner. Eng. 16 (8) (2003) 757–765.
[7] Rafael Teixeira Rodrigues, Jorge Rubio, DAF–dissolved air flotation: potential applications in the mining and mineral processing industry, Int. J. Miner. Process. 82 (2006) 1–13.
[8] Snigdha Khuntia, Subrata Kumar Majumder, Pallab Ghosh, Microbubble-aided water and wastewater purification: a review, Rev. Chem. Eng. 28 (2012) 191–221.
[9] Masayoshi Takahashi, Base and technological application of micro-bubble and nanobubble, Mater. Integration 22 (2009) 2–19.
[10] Koichi Terasaka, Development of microbubble aerator for waste water treatment using aerobic activated sludge, Chem. Eng. Sci. 66 (14) (2011) 3172–3179.
[11] H. Ikeura, F. Kobayashi, M. Tamaki, Removal of residual pesticide, fenitrothion, in vegetables by using ozone microbubbles generated by different methods, J. Food Eng. 103 (3) (2011) 345–349.
[12] Hideki Tsuge, Micro-and Nanobubbles Fundamentals and Applications, Pan Stanford, 2014.
[13] M. Sadatomi, A. Kawahara, K. Kano, A. Ohtomo, Performance of a new micro-bubble generator with a spherical body in a flowing water tube, Exp. Therm. Fluid Sci. 29 (5) (2005) 615–623.
[14] M. Sadatomi, A. Kawahara, H. Matsuura, S. Shikatani, Micro-bubble generation rate and bubble dissolution rate into water by a simple multi-fluid mixer with orifice and porous tube, Exp. Therm. Fluid Sci. 41 (2012) 23–30.
[15] J. Yin, J. Li, H. Li, W. Liu, D. Wang, Experimental study on the bubble generation characteristics for an venturi type bubble generator, Int. J. Heat Mass Tran. 91 (2015) 218–224.
[16] X. Yu, P. Felicia, Optimization of cavitation venturi tube design for pico and nano bubbles generation, Int. J. Mining Sci. Technol. 25 (4) (2015) 523–529.
[17] A. Serizawa, T. Inui, T. Yahiro, Z. Kawara, Laminarization of Micro-bubble Containing Milky Bubbly Flow in a Pipe, 3rd European-Japanese Two-Phase Flow Group Meeting, 2003.
[18] S. Fujikawa, R.S. Zhang, S. Hayama, G.Y. Peng, The control of micro-air-bubble generation by a rotational porous plate, Int. J. Multiphas. Flow 29 (2003) 1221–1236.
[19] C.H. Lee, H. Choi, D.W. Jerng, D.E. Kim, S. Wongwises, H.S. Ahn, Experimental investigation of microbubble generation in the venturi nozzle, Int. J. Heat Mass Tran. 136 (2019) 1127–1138.
[20] J. Huang, L. Sun, M. Dum, Z. Liang, Z. Mo, J. Tang, G. Xie, An investigation on the performance of a micro-scale Venturi bubble generator, Chem. Eng. J., vol. 386, pp 120980.
[21] L. Zhao, L. Sun, Z. Mo, J. Tang, L. Hu, J. Bao, An investigation on bubble motion in liquid flowing through a rectangular Venturi channel, Exp. Therm. Fluid Sci., vol. 97, pp 48-58.
[22] Sakamatapan Kittipong, Mesgarpour Mehrdad, Mahian Omid, Ahn Ho Seon, Wongwises Somchai, Experimental investigation of the microbubble generation using a venturi-type bubble generator, Case Stud. Therm. Eng. 27 (2021) 101238.